Journal of Physics D: Applied Physics

TOPICAL REVIEW • OPEN ACCESS

Progression of group-III sesquioxides: epitaxy, solubility and desorption

To cite this article: Anna Hassa *et al* 2021 *J. Phys. D: Appl. Phys.* **54** 223001

View the article online for updates and enhancements.

You may also like

- The Physical, Structural, Elastic, Optical, and Thermal studies on Sesquioxides (Al2O3, Y2O3,Sb2O3) doped Oxy Fluoro Cobalt Borate Glasses
Ch. Srinivasa Rao, B.K. Sudhakar, N. Ramakrishna Chand et al.

- First-principles study of crystal structure, elastic stiffness constants, piezoelectric constants, and spontaneous polarization of orthorhombic *Pna*2_1-M_2O_3 (M = Al, Ga, In, Sc, Y)
Kazuhiro Shimada

- Passive Q-switching of 2.7 μm Er:Lu_2O_3 ceramic laser with a semiconductor saturable absorber mirror
Xiaojing Ren, Deyuan Shen, Jian Zhang et al.

This content was downloaded from IP address 139.18.118.57 on 03/05/2023 at 15:38

OPEN ACCESS
IOP Publishing
Journal of Physics D: Applied Physics
J. Phys. D: Appl. Phys. **54** (2021) 223001 (15pp)
https://doi.org/10.1088/1361-6463/abd4a4

Topical Review

Progression of group-III sesquioxides: epitaxy, solubility and desorption

Anna Hassa, Marius Grundmann and Holger von Wenckstern

Universität Leipzig, Felix-Bloch-Institut für Festkörperphysik, Linnéstraß e 5, 04103 Leipzig, Germany

E-mail: anna.hassa@uni-leipzig.de

Received 6 October 2020, revised 15 November 2020
Accepted for publication 17 December 2020
Published 9 March 2021

Abstract

In recent years, ultra-wide bandgap semiconductors have increasingly moved into scientific focus due to their outstanding material properties, making them promising candidates for future applications within high-power electronics or solar-blind photo detectors. The group-III-sesquioxides can appear in various polymorphs, which influences, for instance, the energy of the optical bandgap. In gallium oxide, the optical bandgap ranges between 4.6 and 5.3 eV depending on the polymorph. For each polymorph it can be increased or decreased by alloying with aluminum oxide (8.8 eV) or indium oxide (2.7–3.75 eV), respectively, enabling bandgap engineering and thus leading to an extended application field. For this purpose, an overview of miscibility limits, the variation of bandgap and lattice constants as a function of the alloy composition are reviewed for the rhombohedral, monoclinic, orthorhombic and cubic polymorph. Further, the effect of formation and desorption of volatile suboxides on growth rates is described with respect to chemical trends of the discussed ternary materials.

Keywords: Ga_2O_3 thin films, pulsed laser deposition, ternary alloy, desorption of volatile suboxides

(Some figures may appear in colour only in the online journal)

1. Introduction

In the last decades, an increasing number of studies on ultra-wide bandgap semiconductors have been reported and more and more oxide semiconductors have come into focus. In this process a variety of publications and reviews on structural, optical and electrical properties of monoclinic β-Ga_2O_3 [1–5] appeared. Up to now, successful implementations of β-Ga_2O_3 based devices, such as high-power switches and transistors [2–4, 6], solar-blind photo detectors [7], gas sensors [8], or thin film transistors [1], have been reported. The group-III-sesquioxides and their ternary alloys can crystallize in different crystal structures. The growth of the respective structure can be specifically influenced by the choice of growth parameters (e.g. substrate temperature, pressure, metal flux, etc), substrate material and orientation, additional doping (e.g. tin for the orthorhombic polymorph), or others. The electrically insulating Al_2O_3 grows in thermodynamic equilibrium in a rhombohedral crystal lattice where it has a very large optical bandgap of 8.7–8.8 eV. Due to its optical transparency, high temperature and chemical stability, high mechanical strength [9] and its low cost industrial manufacturing capabilities, α-Al_2O_3 is used commonly as substrate material. Binary Ga_2O_3 can be synthesized in four different polymorphs identified as rhombohedral α-, monoclinic β-, defective spinel γ-, or orthorhombic κ-phase (also referred to as ε). Often a cubic δ-phase [10] is mentioned, but Playford *et al* showed that this polymorph is just a nanocrystalline form of

Original Content from this work may be used under the terms of the Creative Commons Attribution 4.0 licence. Any further distribution of this work must maintain attribution to the author(s) and the title of the work, journal citation and DOI.

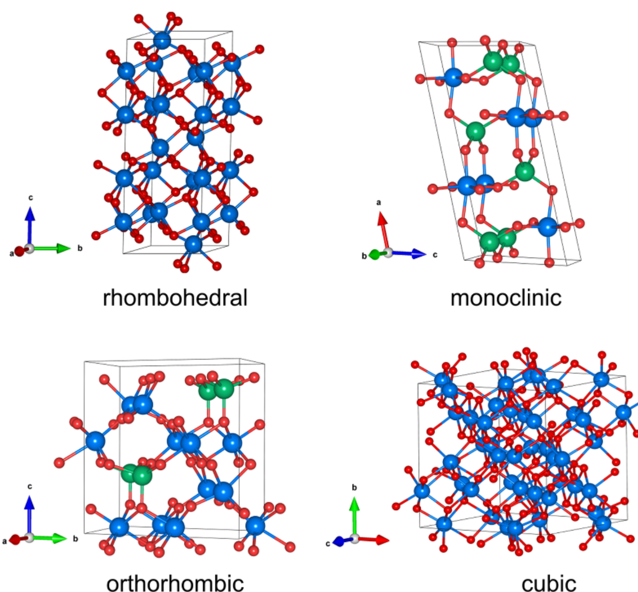

Figure 1. Ball-and-stick representation of the rhombohedral (corundum) α-, the monoclinic β-gallia, the orthorhombic κ-, and the cubic bixbyite crystal structure. The blue marked atoms denote the octahedral (O_h) and the green ones the tetrahedral (T_d) cation sites. The red atoms indicate the oxygen atoms. The structure models were created with VESTA [15].

ε-Ga_2O_3 and not a distinct polymorph [11]. The monoclinic β-gallia structure is the thermodynamically most stable phase for which high-quality bulk single crystals are commercially available and hence most Ga_2O_3 based publications deal with the β-gallia polymorph. The remaining polymorphs are metastable and can change their structure at different transition temperatures, resulting in a ranking of their thermodynamical stability described by $\beta > \kappa > \alpha > \gamma$ [10]. Depending on the polymorph, the bandgap of Ga_2O_3 can range between 4.6 and 5.3 eV. The group-III sesquioxide with the smallest direct bandgap is In_2O_3 with 3.6–3.8 eV [12–14], which crystallizes in the cubic bixbyite structure in thermodynamical equilibrium. Ball-and-stick models of the rhombohedral, monoclinic, orthorhombic and cubic polymorphs are presented in figure 1. In table 1 the space groups, lattice constants and optical bandgap energies of the binary materials, originating in these polymorphs, are summarized.

The fabrication of Ga_2O_3 thin films can be realized by a variety of growth techniques such as mist chemical vapour deposition (mist CVD) [17, 24–31], metal organic CVD (MOCVD) [22, 32–45], halide vapour phase epitaxy (HVPE) [46–56], metalorganic vapour phase epitaxy (MOVPE) [57–59], pulsed laser deposition (PLD) [57, 60–69], molecular beam epitaxy (MBE) [57, 70–76], atomic layer deposition (ALD) [77–79], mist epitaxy [80], the sol–gel method [81], and magnetron sputtering [82]. Besides, crystalline β-Ga_2O_3 bulk crystals can be grown by floating-zone (FZ) [83–85], the edge-defined film-fed growth (EFG) [86], the Czochralski (CZ) [87, 88], the Verneuil [89, 90] and the flux [20, 91–93] methods. In studies about In_2O_3, the semiconductor was inter alia fabricated by MOCVD [94–96], PLD [97–101], MBE [102–107], or sputtering [108–110]. The growth of bulk In_2O_3 from melt was developed and described by the IKZ Berlin [111]. The growth techniques of the ternary alloys used for $(Al,Ga,In)_2O_3$ are summarized for the α-, β-, κ- and cubic bixbyite phase in table 2.

In the present work we review the dependencies of lattice constants and optical bandgaps as a function of the alloy composition of the rhombohedral, monoclinic, orthorhombic, and cubic group-III-sesquioxide polymorphs. The review contains published data as well as own results that we obtained on our thin films grown by PLD. Furthermore, we point out how formation and desorption of volatile suboxides influence the cation composition and under which growth conditions in the PLD chamber desorption can be suppressed. In the course of this, we present thin films with a lateral varying composition, including a short description of the combinatorial PLD approach used.

2. Combinatorial thin film synthesis

Investigations of entire mixtures of ternary solid-solutions within a single thin film sample of ternary $(Al,Ga)_2O_3$ or $(In,Ga)_2O_3$ is possible by employing a composition spread approach, e.g. by pulsed laser deposition (PLD). A combinatorial PLD thin film synthesis was introduced by the semiconductor physics group of the Universität Leipzig (UL) [148], which allows the growth of thin films that exhibit a lateral variation of the cation composition. For a thin film with a compositional gradient, a two-fold segmented target has to be utilized. A synchronized rotation speed of target and substrate used in the PLD chamber is a precondition for our approach. The geometric arrangement of target and substrate influences the cation composition as described in detail in [149].

In general, these thin films were synthesized by employing a KrF excimer laser (248 nm) with an energy density of 2.6 J cm^{-2} on the target surface. The ceramic targets used are composed of one half of Ga_2O_3 (purity 99.999%, Alfa Aeser) and one half of Al_2O_3 (purity 99.997%, Alfa Aeser) or In_2O_3 (purity 99.994%, Alfa Aeser), respectively. In addition, the segments can be doped, e.g. to induce electrical conductivity or to stabilize the growth of the κ-phase [76, 69] (tin doping is decisive). The target material is ball-milled and the homogenized powders are sintered in air and high temperatures between 1150 °C and 1350 °C for 72 h, 2 in. diameter c-plane sapphire substrates are placed in a heatable substrate holder located at a distance of 10 cm opposite to the target. The lateral offset between laser spot position on the target and the substrate center is 16–17 mm. Besides the oxygen pressure, the growth temperature in the PLD chamber can be adjusted. Further details on our growth facilities are summarized in [150]. The pulse repetition number of the samples discussed ranges between 25 000 and 30 000 at a pulse frequency of 10 Hz.

The cation distribution was determined by energy-dispersive x-ray spectroscopy (EDX) using a FEI Nova Nanolab 200 equipped with an Ametek EDAX detector. The crystal structure was identified by XRD 2θ-ω scans conducted with a PANalytical X'pert PRO MRD diffractometer equipped with a

Table 1. Space group, lattice parameter and optical bandgap for various binary polymorphs of the group-II sesquioxides.

Structure	Space group	Polymorph	Lattice constants	Optical bandgap
Rhombohedral	$R\bar{3}c$	α-Al_2O_3	$a = 4.7617$ Å [16]; $c = 12.995$ Å [16]	8.7–8.8 eV
		α-Ga_2O_3	$a = 4.9825$ Å [17]; $c = 13.433$ Å [17]	5.2–5.3 eV
		α-In_2O_3	$a = 5.487$ Å [18]; $c = 14.510$ Å [18]	3.7 eV
Monoclinic	$C2/m$	θ-Al_2O_3	$a = 11.854$ Å [19]; $b = 2.904$ Å [19]; $c = 5.622$ Å [19]; $\beta = 103.83°$ [19]	No exp. values
		β-Ga_2O_3	$a = 12.214$ Å [20]; $b = 3.037$ Å [20]; $c = 5.798$ Å [20]; $\beta = 103.83°$ [20]	4.6–5.0 eV
Orthorhombic	$Pna2_1$	κ-Al_2O_3	$a = 4.8437$ Å [21]; $b = 8.3300$ Å [21]; $c = 8.9547$ Å [21]	No exp. values
		κ-Ga_2O_3	$a = 5.046$ Å [22]; $b = 8.702$ Å [22]; $c = 9.283$ Å [22]	4.9 eV
Cubic	$Ia3$	c-In_2O_3	$a = 10.117$ Å [23]	3.75 eV

Table 2. Growth methods and highest reported cation incorporation for rhombohedral, monoclinic, orthorhombic, and cubic polymorphs of $(Al,Ga,In)_2O_3$ alloys.

Polymorph	Growth method	Reported alloy range
α-$(Al_xGa_{1-x})_2O_3$	Mist CVD [112–115], PLD [116–118], MBE [119]	Entire composition range
α-$(In_yGa_{1-y})_2O_3$	Mist CVD [113, 120, 121]	$y \leq 0.08$, $y \geq 0.67$ [120]
β-$(Al_xGa_{1-x})_2O_3$	PLD [122–125], MBE [126–129], sputtering [130]	$x \leq 0.61$ [128]
β-$(In_yGa_{1-y})_2O_3$	MOCVD [131], PLD [101, 132–135], MBE [71, 75, 136], sol–gel method [137]	$y \leq 0.35$ [138]
κ-$(Al_xGa_{1-x})_2O_3$	Mist CVD [139], PLD [140–142]	$x \leq 0.65$ [140]
κ-$(In_yGa_{1-y})_2O_3$	Mist CVD [143], PLD [144, 145]	$y \leq 0.35$ [144]
c-$(Ga_zIn_{1-z})_2O_3$	MOCVD [146, 147], PLD [134, 132], MBE [138], sol–gel method [137]	$z \leq 0.5$ [146, 147]

PIXcel^{3D} detector with 255 channels operating in 1D scanning line mode. The thin film thickness (d) was determined by spectroscopic ellipsometry employing a dual rotating compensator ellipsometer (RC2, J.A. Woollam M2000) with a spot size of about $300 \times 500\,\mu m^2$. Then the growth rate r was calculated by dividing d by the number of pulses during deposition.

3. Formation and desorption of volatile suboxides

In several publications the influence of growth conditions on growth rates (r) during deposition of Ga_2O_3 and its ternary alloys with In or Al was studied systematically. The investigations revealed that under high growth temperatures (T_g) and oxygen-poor growth conditions volatile suboxides forms and desorbs leading to lower r and that in ternary alloys a non-stoichiometric incorporation of the provided cations into the thin film can be observed.

Vogt *et al* examined the influence of the O- and Me-fluxes (Me = Ga, In) ratio for binary Ga_2O_3 and In_2O_3, respectively, during MBE growth [73, 136]. In Ga_2O_3 for oxygen-rich conditions the growth rates are determined by the offered metal flux and no desorption of cation species was observed, which leads to the assumption that all metal atoms are incorporated into the thin film layer. In a oxygen-poor regime volatile Me_2O suboxides are formed, which were not incorporated into the thin film. Consistent studies of PLD grown Ga_2O_3 thin films also revealed the influence of oxygen pressure ($p(O_2)$) and growth temperature on the growth rate. Lower growth rates are observed for decreasing oxygen pressure [65] or increasing growth temperatures [66], respectively.

In the ternary alloys $(Al,Ga)_2O_3$ and $(In,Ga)_2O_3$ the desorption of volatile suboxides manifests itself in such a way that, besides decreasing r, the cation ratio of Al to Ga or In to Ga is altered. For PLD grown $(Al,Ga)_2O_3$ thin films a high growth temperature and/or low oxygen pressure result in lower r and higher Al incorporation into the layer [123, 124, 142, 151]. Due to the lower dissociation energy of the Ga–O bond compared to the Al–O bond, in an oxygen poor regime Ga atoms form volatile sub-oxides being desorbed, which leads to a preferential incorporation of the Al atoms. In the $(In,Ga)_2O_3$ alloy desorption of volatile suboxides can be observed, too [131, 136]: the Ga atoms are preferentially incorporated on account of the higher dissociation energy of the Ga–O bond

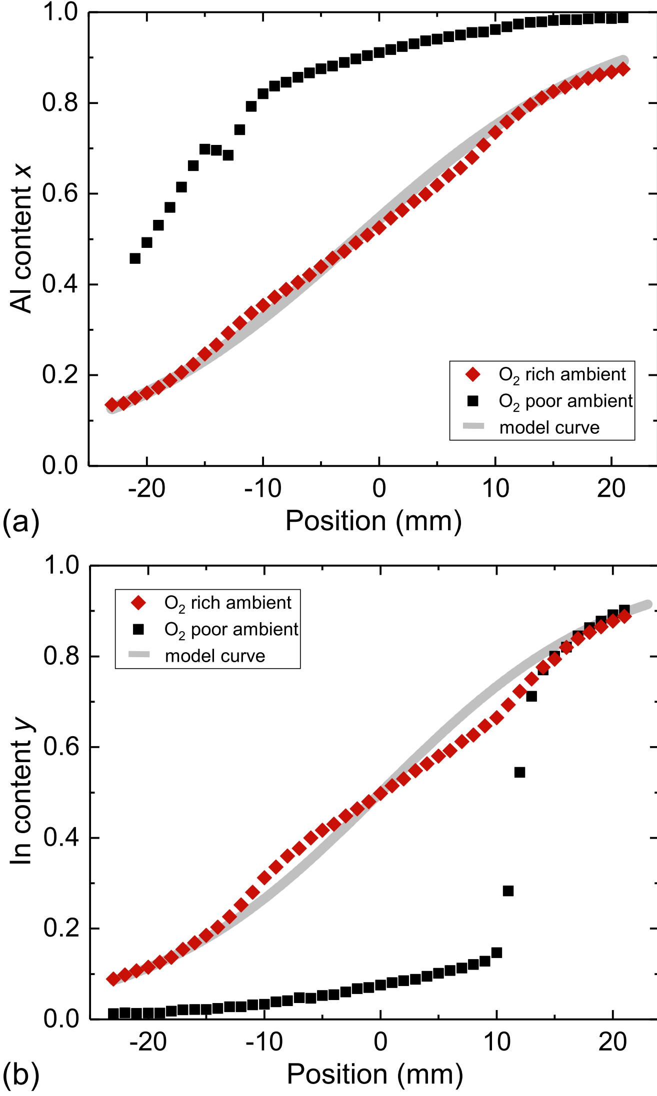

Figure 2. (a) Al cation ratio x and (b) Al cation ratio y recorded along the gradient direction of CCS-PLD $(Al_xGa_{1-x})_2O_3$ and $(In_yGa_{1-y})_2O_3$ thin films on c-sapphire substrates. The growth temperature of each sample was around 640 °C and the oxygen regimes are indicated in the graphs.

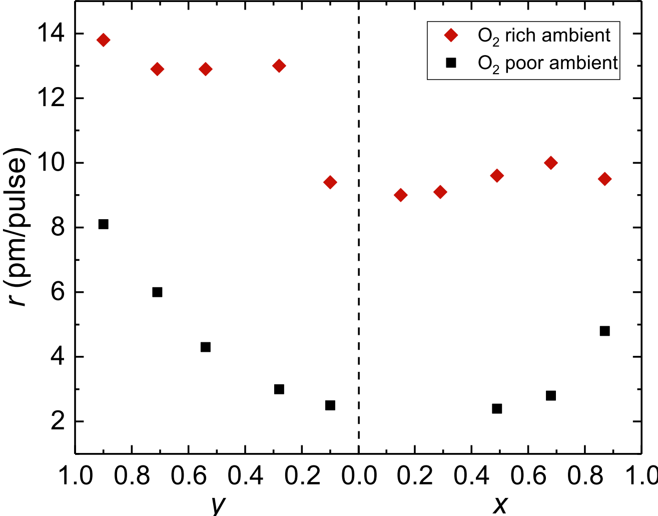

Figure 3. Growth rates r for different cation compositions of $(Al_xGa_{1-x})_2O_3$ and $(In_yGa_{1-y})_2O_3$ thin films grown on c-plane sapphire at 640 °C and oxygen rich ($p(O_2)$ = 0.01 mbar) or poor ($p(O_2)$ = 0.0003 mbar) conditions, respectively.

compared to the In–O bond. In addition, a metal-exchange has to be taken into account for this alloy. In $(In,Ga)_2O_3$ the Ga atoms etches already existing In–O bonds and then replace In [136]. As a result, the released In atoms form either droplets on the thin film surface at low T_g or will be desorbed as In_2O suboxide at high T_g, leading to a further reduction of the In incorporation as well as lower growth rates [136]. To investigate systematically the influence of $p(O_2)$ on $(Al,Ga)_2O_3$ and $(In,Ga)_2O_3$, CCS-PLD thin films grown with well-defined lateral variation of the cation flux at a constant temperature of 640 °C and either an oxygen poor regime of $p(O_2)$ = 0.0003 mbar or an oxygen rich regime of $p(O_2)$ = 0.01 mbar on c-plane sapphire were studied. The composition gradients were determined by EDX and the resulting Al and In contents in terms of the gradient position are presented in figure 2. Position 0 indicates the center of the wafer and the gray solid lines, the calculated model curve of the CCS-PLD approach [149].

For oxygen rich conditions, the spatial resolution of the alloy composition fits quite well to the model curve, which indicates a stoichiometric target-to-layer transfer with growth rates between 9 and 10 pm/pulse for all Al contents and low In content ($y = 0.1$). For higher y the growth rates range between 12.9 and 13.8 pm/pulse as visible in figure 3. In an oxygen poor regime a strong deviation from the stoichiometric cation incorporation in $(Al,Ga)_2O_3$ and $(In,Ga)_2O_3$, respectively, can be observed as well as a strong decrease in growth rates. For the $(Al,Ga)_2O_3$ sample the Al content increases suddenly in the first quarter from 45 at.% to around 80 at.% and increases in the last three quarters slightly up to 99 at.%. The narrow Al valley at position −14/−13 is caused by phase separation, which is not within the scope of this work for which reason this is not discussed further. A similar behaviour is given for the $(In,Ga)_2O_3$ sample: for oxygen poor conditions the In content increases in the first three quarters only up to approximately 20 at.% and jumps in the last quarter up to 80 at.% (see figure 2).

The strong non-stoichiometric cation incorporation is caused by the low supply of oxygen atoms during growth leading to the formation and subsequent desorption of volatile suboxides, which can be further approved by the low grates being ≈6–7 pm/pulse below the values of the oxygen rich samples. The growth rates of the $(In,Ga)_2O_3$ sample in the oxygen regime increases with increasing In content, which is caused on the one hand by the higher ionic radii of In compared to Ga and on the other hand by a kinetically favored formation of In_2O_3 leading to a faster reaction with O_2 and thereby to higher r.

Interestingly, the cation ratio of the $(In_xGa_{1-x})_2O_3$ thin film fits in the last quarter ($y > 0.6$) with the model curve due to an observable phase separation to the cubic bixbyite phase

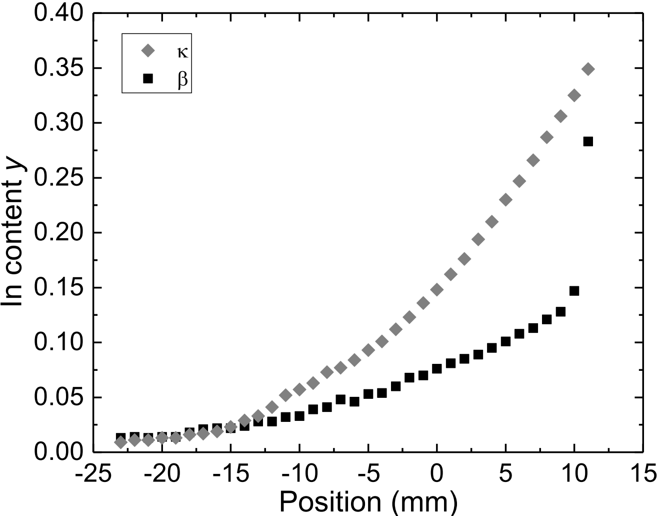

Figure 4. In content y in terms of the spatial location on the wafer for a β- and a κ-$(In_yGa_{1-y})_2O_3$ thin film on c-plane sapphire. Both thin films were deposited in an oxygen poor regime ($p(O_2)$ = 0.0003 mbar) at $T_g = 640\,^\circ$C.

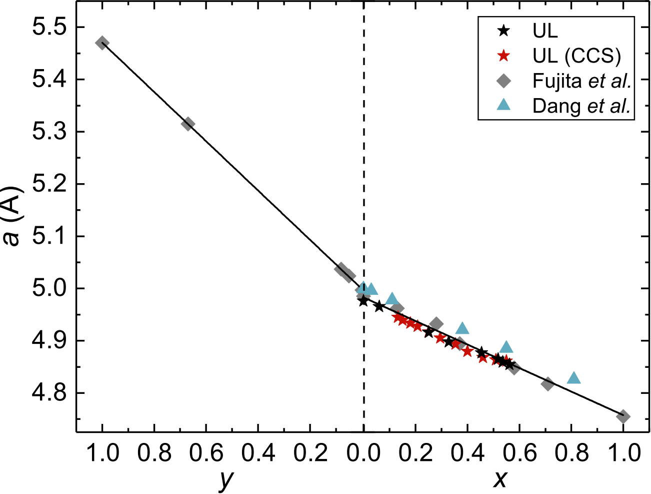

Figure 5. Lattice constant a of α-$(In_yGa_{1-y})_2O_3$ and α-$(Al_xGa_{1-x})_2O_3$ as a function of the alloy composition. The data was taken from Hassa *et al* [118], Fujita and Kaneko [113] and Dang *et al* [115]. Recent data from our PLD thin films are shown by star-shaped (for lateral homogeneous thin films) or diamond-shaped (for CCS-PLD) markers and are denoted by UL.

(for further details see [132]), which allows the assumption that despite formation and desorption of volatile suboxides, both, Ga and In, are incorporated stoichiometrically in this phase.

In summary, it has been shown in this part that in the $(In,Ga)_2O_3$ alloy mainly In_2O forms and desorbs, why proportionately more Ga atoms are detected in the layer. Against it, in the $(Al,Ga)_2O_3$ alloy the significantly higher Al incorporation is due to a stronger Ga_2O formation and desorption.

Studies of the influence of T_g and $p(O_2)$ on β- and κ-$(Al,Ga)_2O_3$ thin films, published in [151, 142], demonstrate that desorption occurs for both polymorphs. A direct comparison showed that the formation and desorption of volatile suboxides is stronger in the monoclinic alloy, resulting in an increased Al incorporation in the layer under same growth conditions. A potential reason for the slightly suppressed desorption in the orthorhombic polymorph is surfactant-mediated growth. An additional tin supply during growth, both for PLD and MBE is necessary to synthesize orthorhombic thin films [69, 76]. Tin acts as a surfactant in the growth process and is not incorporated into the thin film [69, 141].

Figure 4 presents β- and κ-$(In,Ga)_2O_3$ thin films grown at $T_g = 640$ °C and oxygen poor conditions ($p(O_2)$ = 0.0003 mbar). The κ-$(In,Ga)_2O_3$ thin film was already discussed in [144] and a comparable β-$(In,Ga)_2O_3$ thin film in [132] by the University of Leipzig (UL). The β-phase crystallized up to approximately $y = 0.28$ and the κ-phase up to $y = 0.35$. For higher In contents phase separation proceeds to the hexagonal InGaO (II) as well as to the cubic $(Ga,In)_2O_3$ phase (crystal structure determined by x-ray diffraction [132, 144]). From position -23 to -12, the increase of y of both polymorphs is equal. After this point it can be observed that the content gap of y becomes larger with ongoing positions. At position 11 the gap is $\Delta y = 0.17$, which indicates a more extensive formation and desorption of volatile suboxides in the β-phase.

4. Crystal structure

The group-III sesquioxides (Al_2O_3, Ga_2O_3 and In_2O_3) have different ground state crystal structures, namely the rhombohedral corundum, the monoclinic β-gallia and the cubic bixbyite structure, respectively. The rhombohedral corundum-structure has been reported as the only polymorph for all of the group-III sesquioxides and hence it should in principle be possible to stabilize the α-phase throughout the entire composition range [121]. Phase separation in the $(Al,Ga,In)_2O_3$ alloys is expected for all other polymorphs. The miscibility gap will likely depend on the polymorph considered. In table 2 the actual reported maximum cation compositions of the thermodynamically most stable polymorphs are shown. Since Al, Ga and In have different ionic radii the lattice constants will change within ternary alloys. An incorporation of Al into Ga_2O_3 leads to decreasing lattice parameters, while In incorporation causes an increase. The cation sites have a coordination number of 4 or 6 depending on the distinct polymorph. The ratio and arrangement of the octahedral (O_h) or tetrahedral (T_d) lattice sites differs in the polymorphs discussed below and is distinguished by color in figure 1.

4.1. Rhombohedral crystal structure

In the corundum structure (space group $R\bar{3}c$) all Me^{3+} (Me = Al, Ga, In) cations occupy O_h lattice sites and grow within a hexagonal close-packed O^{2-} array. The unit cell presented in figure 1 contains six Me_2O_3 formula units with the space group $R\bar{3}c$. As indicated, all group-III-sesquioxides can be synthesized in the rhombohedral structure and alloying in the whole composition range should be possible as observed for α-$(Al_xGa_{1-x})_2O_3$. It is interesting that so far In in α-Ga_2O_3 has only been

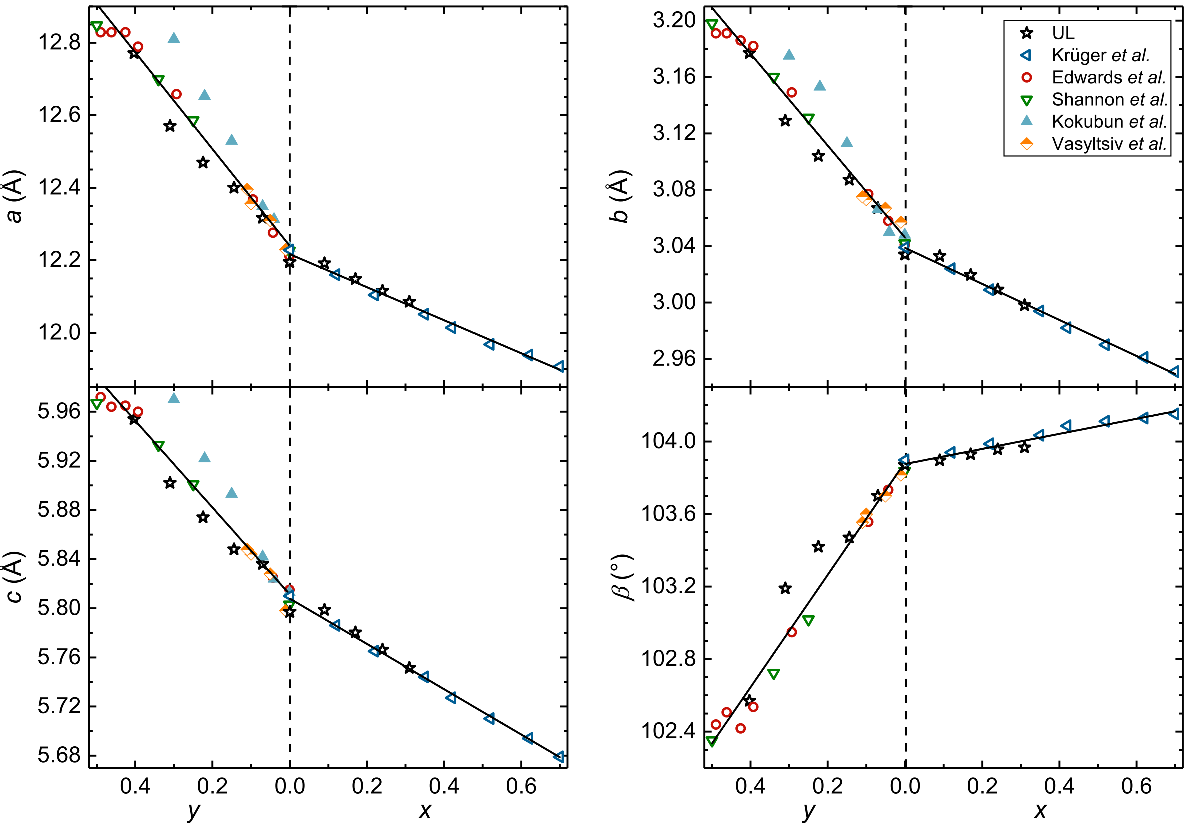

Figure 6. Lattice constants a, b, c and β in dependence on the cation composition for monoclinic β-$(In_yGa_{1-y})_2O_3$ and β-$(Al_xGa_{1-x})_2O_3$. Literature data were compiled for powder samples [23, 92, 152–154], thin films [137] and bulk crystals [155]. The Recent data from our PLD thin films are shown by star-shaped markers and are denoted by UL.

reported up to 8 at.%, while Ga has been incorporated up to 33 at.% into α-In_2O_3 [120]. The pseudo-hexagonal lattice constants (a/c) in the corundum-structured $(Al,Ga,In)_2O_3$ thin films range between $a = 4.7617$ Å/$c = 12.995$ Å [113] for Al_2O_3, $a = 4.9825$ Å/$c = 13.433$ Å for Ga_2O_3 [17], and $a = 5.487$ Å/$c = 14.510$ Å for In_2O_3 [18]. Figure 5 presents the evolution of the a-lattice constant as a function of the composition for relaxed thin films [113, 115, 118], which follow Vegard's law. The linear fit of the a-lattice constant can be found in table 3. The slope in β-$(In_yGa_{1-y})_2O_3$ is much higher than for β-$(Al_xGa_{1-x})_2O_3$ due to a higher relative percentage difference in the atomic radii of In with respect to Ga (14% larger) compared to Al to Ga (6.5% smaller).

4.2. Monoclinic β-gallia crystal structure

Monoclinic β-Ga_2O_3 belongs to space group $C2/m$ [20] and the unit cell is formed by four Ga_2O_3 molecules, where the Ga atoms occupy either the O_h or the T_d lattice site with a ratio of 1:1. By alloying β-Ga_2O_3 with In or Al, these cations prefer the O_h lattice sites [92, 154]. After Al has occupied all O_h lattice sites (50 at.%), the T_d lattice sites are then also occupied [154]. There exist three possibilities of connections between the octahedrally and tetrahedrally ordered cations. In the [010]-direction the T_d are connected with each other as well as the O_h. The O_h are also connected along the [102]-direction. In the remaining directions, there exists only linkings between the T_d and O_h cation sites [156]. The oxygen atoms can occupy three different lattice sites, two of them, namely O(1) and O(2), are threefold and O(3) is fourfold coordinated.

Since only Ga_2O_3 crystallizes in the β-phase, the solubility of Al and In in this structure is limited. The highest reported Al content in β-$(Al_xGa_{1-x})_2O_3$ thin films is $x = 0.61$

Table 3. Dependence of the lattice constants of rhombohedral, monoclinic, orthorhombic, and cubic $(Al,Ga,In)_2O_3$ thin films on the cation incorporation. The equations represent the linear fittings from figures 5–7 and [23, 158, 159].

Material	Lattice parameter
α-$(Al_xGa_{1-x})_2O_3$	$a(x) = (4.983 - 0.225x)$ Å
α-$(In_yGa_{1-y})_2O_3$	$a(y) = (4.999 + 0.471y)$ Å
β-$(Al_xGa_{1-x})_2O_3$	$a(x) = (12.217 - 0.455x)$ Å
	$b(x) = (3.039 - 0.128x)$ Å
	$c(x) = (5.808 - 0.184x)$ Å
	$\beta(x) = (103.88 + 0.415x)$ Å
β-$(In_yGa_{1-y})_2O_3$	$a(y) = (12.241 + 1.332y)$ Å
	$b(y) = (3.046 + 0.325y)$ Å
	$c(y) = (5.812 + 0.353y)$
	$\beta(y) = (103.88 - 3.098y)$ Å
κ-$(Al_xGa_{1-x})_2O_3$	$c(x) = (9.274 - 0.347x)$ Å
κ-$(In_yGa_{1-y})_2O_3$	$c(y) = (9.268 + 1.121y)$ Å
c-$(Ga_zIn_{1-z})_2O_3$	$a(z) = (10.113 - 0.803z)$ Å

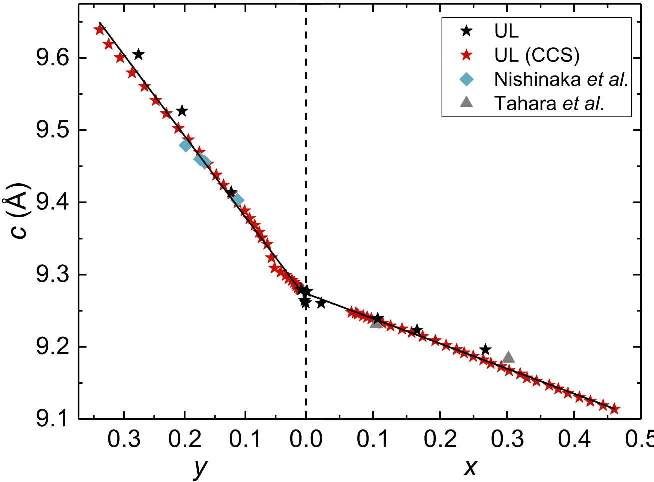

Figure 7. Lattice constant c of κ-$(In_yGa_{1-y})_2O_3$ and κ-$(Al_xGa_{1-x})_2O_3$ as a function of the alloy composition. The data was taken from: Hassa *et al* [144, 141], Kneiß *et al* [145], Nishinaka *et al* [143], Tahara *et al* [139], and Storm *et al* [140].

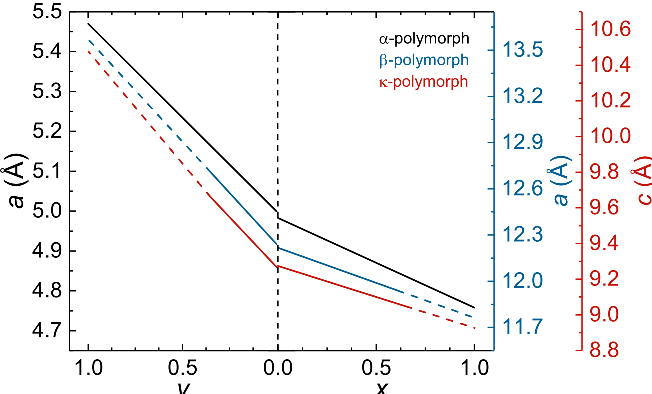

Figure 8. Lattice constants of the rhombohedral, monoclinic and orthorhombic polymorph of $(Al_xGa_{1-x})_2O_3$ and $(In_xGa_{1-x})_2O_3$ as function of the alloy composition. The graphs are based on the equations depicted in table 3. The solid lines mark the maximum experimental cation ratio and the dashed lines are extrapolated to Al_2O_3 ($x = 1$) and In_2O_3 ($y = 1$).

[128] and $x = 0.78$ in ceramic samples [157]. The maximum In incorporation into β-$(In_yGa_{1-y})_2O_3$ thin films is $y = 0.35$ [71] and $y = 0.44$ [23] in ceramic samples. The lattice constants of β-Ga_2O_3 are $a = 12.214$ Å, $b = 3.037$ Å, $c = 5.798$ Å and $\beta = 103.83°$ [20]. Figure 6 presents published lattice parameters of monoclinic $(Al,Ga)_2O_3$ and $(In,Ga)_2O_3$ alloys as a function of the Al or In content, respectively [23, 92, 137, 152, 154, 155]. The data points exhibit a linear dependency and thus follow Vegard's law. The fits of each lattice parameter are shown in table 3. Interestingly, for $x = 0$ the lattice constants are in close agreement with the values of binary β-Ga_2O_3, while for $y = 0$ the lattice constants a, b and c are 1%–1.7% higher. The angle β is for both alloys the same of about 103.88° fitting well to the binary value of 103.83° [20]. Extrapolations to $x = 1$ show a close agreement of the lattice parameters with those of monoclinic θ-Al_2O_3, with the exception of the lattice parameter β, which should be nearly identical for both materials.

4.3. Orthorhombic crystal structure

In the orthorhombic structure the T_d to O_h coordinated cations exhibit a ratio of 1:3 and are formed by six molecules in space group $Pna2_1$. Often the orthorhombic polymorph of Ga_2O_3 is also denoted as ε-phase. Since some literature, probably Cora or Kneiß *et al*, the isostructurality to κ-Al_2O_3 demonstrated, the orthorhombic polymorph is named κ and not ε [22, 69]. The Me^{3+} cations can be arranged as pure O_h or mixed T_d and O_h layer along the [001]-direction or as zigzag ribbons consisting of edge-shared O_h and corner-shared T_d layers [22, 21]. The oxygen atoms arrange themselves as an ABAC pseudo-close-packed stacking [21].

Since the Al_2O_3 can form an orthorhombic lattice, the whole composition range of κ-$(Al_xGa_{1-x})_2O_3$ should be feasible. Actually the highest reported Al content on c-sapphire substrates is $x = 0.46$ [141], which can be significantly increased up to $x = 0.65$ using a κ-Ga_2O_3 buffer layer between substrate and thin film [140]. For κ-$(In_yGa_{1-y})_2O_3$ on c-sapphire a maximum In incorporation of $x = 0.35$ [144] was realized, up to now.

The lattice constants for κ-Al_2O_3 are identified to be $a = 4.8437$ Å, $b = 8.3300$ Å and $c = 8.9547$ Å [21] and for κ-Ga_2O_3 as $a = 5.046$ Å, $b = 8.702$ Å and $c = 9.283$ Å [22]. The influence of the Al content [139–141] or rather In content [143–145] on the lattice parameter c is presented in figure 7. As for the monoclinic alloys causes the Al (In) incorporation a linear decrease (increase) of c according to Vegard's law. Linear fittings of the experimental values results in the equations listed in table 3. Assuming again $x = 0$ and $y = 0$, c fits well with the experimental result of binary κ-Ga_2O_3. By extrapolating the lattice constant up to $x = 1$, 8.927 Å is obtained being in close agreement with binary κ-Al_2O_3 [21], too.

4.4. Cubic crystal structure

The cubic structure, also called bixbyite, is body-centered cubic (bcc) and belongs to the space group $Ia3$. The bcc unit cell consists of 16 molecules. The sixfold coordinated cations can occupy the Wyckhoff position 8b (cation lies on the space diagonal between two oxygen vacancies) or the Wyckhoff position 24d (within the bcc cell with the oxygen vacancies located on the surface diagonal), respectively. The ratio of the b to d cation positions is 8:24 in the unit cell. As substrates (100)ZrO_2 or (006)Al_2O_3 are mostly used. The solubility limit of Ga atoms into phase pure cubic In_2O_3 is 50 at.% [146, 147]. For higher Ga contents an additional phase, usually the monoclinic β-gallia and/or hexagonal $InGaO_3$ phase can be observed. The lattice parameter in binary In_2O_3 is $a = 10.117 \pm 0.001$ Å [158] and can be decreased by alloying with Ga [23, 159] following for the a-lattice constant Vegard's law presented in table 3.

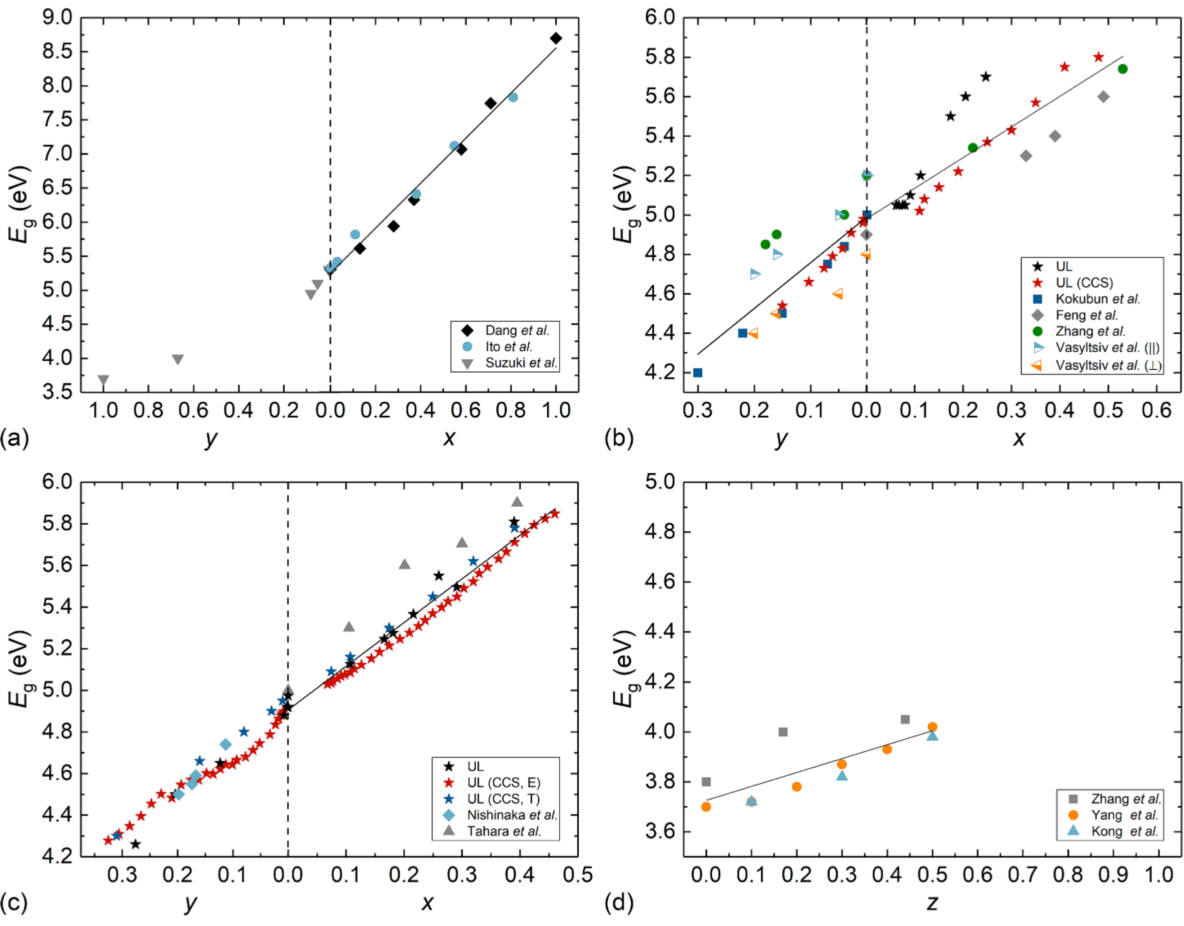

Figure 9. Optical bandgap as function of the Al, In or Ga incorporation x, y or z for the (a) rhombohedral, (b) monoclinic, (c) orthorhombic and (d) cubic polymorphs of the group-III sesquioxides. The data were extracted for the α-polymorph from [112, 115, 120], for β- from [122, 133, 134, 137, 151, 155, 160, 161], for κ- from [139–141, 143–145], and for the cubic phase from [134, 146, 147].

Table 4. Linear fits of the optical bandgaps in dependence on the Al incorporation x or In content y for the α-, β-, κ- and cubic phase of $(Al,Ga,In)_2O_3$. The data are taken for α from [115, 112], for β from [122, 133, 134, 137, 155, 160, 161], and for κ from [139–141, 143–145].

Material	Bandgap (eV)
α-$(Al_xGa_{1-x})_2O_3$	$E_g(x) = 5.25 + 3.31x$
β-$(Al_xGa_{1-x})_2O_3$	$E_g(x) = 4.98 + 1.56x$
β-$(In_yGa_{1-y})_2O_3$	$E_g(y) = 4.99 - 2.32y$
κ-$(Al_xGa_{1-x})_2O_3$	$E_g(x) = 4.91 + 2.10x$
κ-$(In_yGa_{1-y})_2O_3$	$E_g(y) = 4.90 - 1.95y$
c-$(Ga_zIn_{1-z})_2O_3$	$E_g(z) = 3.73 + 0.56z$

5. Optical bandgap

One of the most important aspects of the group-III sesquioxides is the possibility of bandgap engineering in a broad range. Actually, Al_2O_3 and Ga_2O_3 are indirect semiconductors, but with such a small difference in the band-to-band transition that both behave much as direct bandgap semiconductors [3, 162]. For In_2O_3 a distinct classification of direct or indirect bandgap is also possible and widely discussed. As introduced by Weiher and Ley, In_2O_3 can exhibit an indirect, forbidden band-to-band transition of $E_g^{\text{indirect}} = 2.62$ eV and a direct transition of $E_g^{\text{direct}} = 3.75$ eV [13]. Further investigations of Walsh *et al* showed that the direct optical band-to-band transitions are parity-forbidden, resulting in an upper bandgap limit of 2.9 eV [163]. The first dipole allowed band-to-band transition can be observed at 3.7 eV, which could be experimentally confirmed [164, 13].

For Ga_2O_3 the bandgap energy depends strongly on the respective formed polymorph. For instance, the bandgap of the monoclinic polymorph can range between 4.6 and 5.0 eV [3]. Due to the optical anisotropy, the bandgap depends strongly on the orientation and polarization [166]. The orthorhombic Ga_2O_3 exhibits an optical bandgap of 4.9 eV [38, 55, 69] and the rhombohedral phase a slightly higher one of 5.2–5.3 eV [24, 46, 48, 58]. The optical bandgap of α-Al_2O_3 was found to be 8.7–8.8 eV [115, 167] and for binary κ-Al_2O_3 no experimental bandgaps are available. Figure 9 summarizes experimental results of optical bandgaps as a function of the alloy composition for rhombohedral (α), monoclinic (β), orthorhombic (κ) and cubic polymorphs of $(Al,Ga,In)_2O_3$ thin films. The linear fits of the separate polymorphs are summarized in table 4. The highest bandgap variance is observed in the rhombohedral α-phase, since each sesquioxide can crystallize in the rhombohedral structure

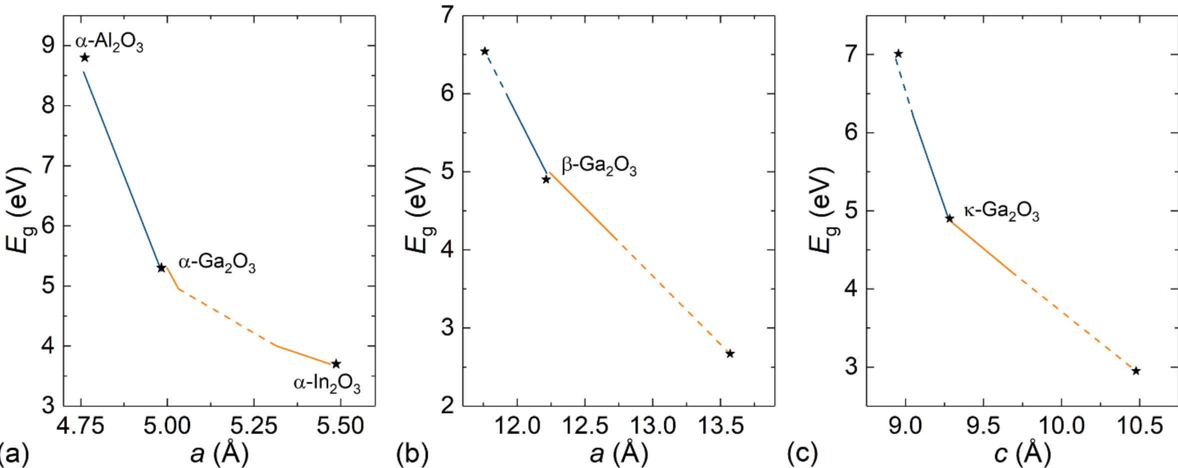

Figure 10. Optical bandgap in dependence on the lattice parameter (a) a for rhombohedral, (b) a for monoclinic and (b) c for orthorhombic $(Al,Ga)_2O_3$ and $(In,Ga)_2O_3$. The solid line presents linear fittings of recently published data. The dashed lines shows the extrapolation to binary Al_2O_3 and In_2O_3. The lattice parameters and bandgap energies for α-, β- and κ-Ga_2O_3 as well as for α-Al_2O_3 and In_2O_3 are taken from table 1.

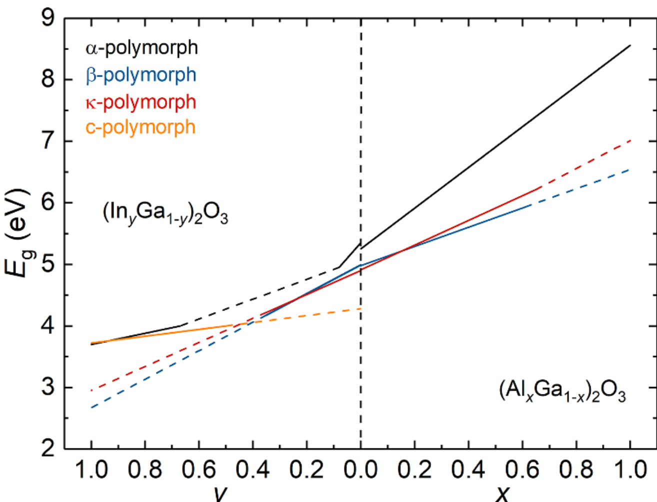

Figure 11. Optical bandgap in dependence on the cation incorporation x or y based on table 4 for the rhombohedral (black), monoclinic (blue), orthorhombic (red) and cubic polymorphs (orange) of the sesquioxides. The solid lines represents the maximum reported cation incorporation for the distinct polymorphs and the dashed lines are extrapolated to the binary sesquioxides. Reprinted by permission from Springer Nature Customer Service Centre GmbH: [Springer Nature] [Springer eBook] [165], (2020).

allowing bandgap engineering between 3.7 eV [120] and 8.7 eV [115], except a range of $4 < E_g < 4.95$ eV [120]. For the β- and κ-phase alloys is the bandgap engineering limited by the solubility and therefore phase separation.

Using the linear fits (see table 4), extrapolations to the current maximum Al and In incorporation allows declaration of the possible bandgap engineering. It follows that for β-$(Al,Ga,In)_2O_3$ thin films the bandgap can be varied between approximately 4.2 and 5.9 eV corresponding to an In content of 35 at.% and an Al content of 61 at.% into β-Ga_2O_3. For the ternary alloys of the orthorhombic structure ensues a similar range of about 4.25–6.2 eV (35 at.% In, 65 at.% Al). For phase pure cubic $(Ga_zIn_{1-z})_2O_3$ amounts the maximum reported Ga incorporation $z = 0.5$ [146, 147] leading to a small bandgap variation of 3.7–4.05 eV. Figure 11 illustrates the actual possible and extrapolated bandgap energies of all polymorphs discussed in dependence on the alloy compound. In addition, figure 10 summarizes the data fits from tables 3 and 4 for α-, β- and κ-Ga_2O_3 alloyed with Al or In and represents the relation of the optical bandgap as a function of the lattice parameter. For this purpose, these equations were resolved according to x/y and then put on a par. Assuming that monoclinic and orthorhombic $(Al,Ga,In)_2O_3$ thin films are achievable up to binary Al_2O_3 and In_2O_3, the plots (E_g vs. x/y and E_g vs. lattice constant) were extrapolated up to the maximum and minimum possible values of $x = 1$ or $y = 1$ (dashed lines in figure 11), respectively. As a result of these extrapolations for the monoclinic phase a maximum bandgap range of 2.67–6.54 eV and for the orthorhombic polymorph a range of 2.95–7.01 eV. Compared with experimental results of α-Al_2O_3 (8.7–8.8 eV [115, 167]), the extrapolated monoclinic and orthorhombic Al_2O_3 bandgaps are much smaller. The extrapolated values for β-In_2O_3 reflect the value of the parity-forbidden direct bandgap of cubic In_2O_3, whereby the extrapolated value of κ-In_2O_3 is near the fundamental bandgap [163].

In contrast, the alloy of cubic In_2O_3 with Ga exhibits direct band-to-band transitions with a possible bandgap range of 3.7 eV to an extrapolated maximum of 4.28 eV for cubic Ga_2O_3. A possible reason for the strong difference of the extrapolated values for β- and κ-In_2O_3 with the actual cubic In_2O_3 bandgaps can be that the calculation for the β- and κ-polymorph starts at the Ga_2O_3 of the phase diagram where no parity-forbidden transitions were reported. Since the graphs intersect each other at an average In content of 40 at.%, this could indicate the critical cation composition where phase separations proceeds.

However, for α-$(In,Ga)_2O_3$ and cubic $(Ga,In)_2O_3$ thin films, a bandgap bowing of $b = 1.69$ eV [168] can be observed

resulting in a minimum bandgap of 3.7 eV [113, 120, 146]. Such a bowing cannot be excluded for the monoclinic and orthorhombic polymorph, so it should be kept in mind for higher potential In contents.

6. Summary and outlook

In this report, we pointed out that for the group-III-sesquioxides, oxygen pressure has a strong influence on the alloy composition and cation incorporation of PLD grown thin films. At low oxygen pressures, volatile suboxides are formed and desorb. Due to different dissociation energies of the Me–O bonds, the provided cations are incorporated with different preferences. The dissociation energy of the Al–O bond is higher as the Ga–O bond, which is higher than the In–O bond, resulting in a preferentially incorporation of Al into the $(Al,Ga)_2O_3$ alloy or Ga into the $(In,Ga)_2O_3$ alloy.

Besides, we have reviewed the dependence of lattice constants and optical bandgap on the group-III sesquioxide alloy composition for the rhombohedral, monoclinic, orthorhombic, and cubic crystal structures. The summarized data revealed different solubility limits of the distinct polymorphs of $(Al_xGa_{1-x})_2O_3$ and $(In_yGa_{1-y})_2O_3$ due to different ground state crystal structures of the binary materials. For instance, in the rhombohedral structure the cation incorporation of Ga in α-Al_2O_3 or Al in α-Ga_2O_3 is possible in the entire compositional range, while Ga in α-In_2O_3 was only reported up to 33 at.% and In in α-Ga_2O_3 has a solubility limit of around 8 at.%. For the monoclinic and orthorhombic polymorphs of Ga_2O_3, which are not reported for binary Al_2O_3 and In_2O_3, the maximum reported cation incorporations are similar: the Al content reaches a maximum of 61–65 at.% and In is included up to 35 at.% in β- or κ-Ga_2O_3. The highest reported Ga content in the cubic In_2O_3 phase was reported to be 50 at.%. Starting from Ga_2O_3 the lattice constants decreases (increases) with increasing Al (In) incorporation and follow for all reviewed polymorphs Vegard's law. We also reviewed the evolution of the bandgap, which leads to bandgap ranges from 3.7–4 and 4.95–8.7 eV for the α-polymorph, 4.2–5.9 eV for the β-polymorph, 4.2–5.7 eV for the κ-polymorph, and 3.7–4.05 eV for the cubic phase. The bandgaps and corresponding miscibility limits are summarized in figure 12 for all polymorphs discussed.

Future studies and investigations should continue to focus on expanding the phase limits of the ternary alloys for each polymorph of the group-III sesquioxides. Since the α-phase can be stabilized across the entire composition range of the $(Al,Ga)_2O_3$ alloy and this is also—at least theoretically—feasible for the $(In_xGa_{1-x})_2O_3$ alloy, this structure is particularly suitable for the realization of wavelength-selective photodetectors, such as deep UV-photodetectors or QWIP's. With the availability of native β-Ga_2O_3 substrates, alloys of this phase are a prime candidate for the realization of high performance power devices and possibly QWIP's. The κ-phase is due to it is spontaneous polarization especially interesting for confining extremely high 2DEG densities, which can be potentially exploited in HEMT's. The emphasis should also remain on optimizing or realizing the electrical conductivity of all polymorphs of $(In_xGa_{1-x})_2O_3$ or $(Al_xGa_{1-x})_2O_3$, respectively.

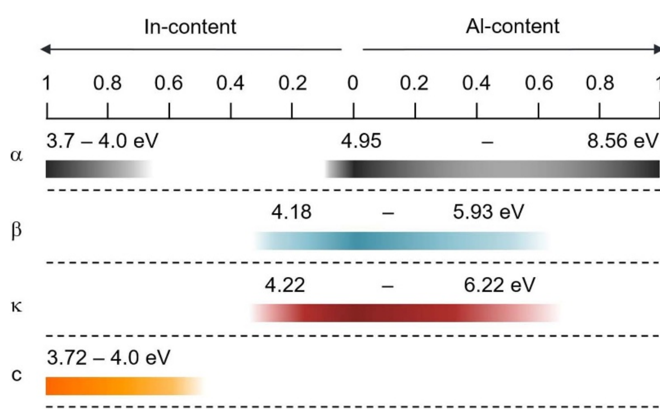

Figure 12. Current miscibility limits and corresponding optical bandgap energies for the rhombohedral α-, monoclinic β- and orthorhombic κ-polymorph of $(Al_xGa_{1-x})_2O_3$ and $(In_yGa_{1-y})_2O_3$ as well as for cubic $(In_yGa_{1-y})_2O_3$. Reprinted by permission from Springer Nature Customer Service Centre GmbH: [Springer Nature] [Springer eBook] [165], (2020).

Acknowledgments

We thank Monika Hahn for PLD target fabrication, Jörg Lenzner and Daniel Splith for EDX measurements, and Chris Sturm for the determination of the thin film thicknesses using ellipsometry. This work was supported by European Social Fund within the Young Investigator Group 'Oxide Heterostructures' (No. SAB 100310460). This work was funded by the Deutsche Forschungsgemeinschaft (DFG, German Research Foundation)-Project Number 31047526, SFB762, project B04. A H acknowledge the Leipzig School for Natural Sciences BuildMoNa. We acknowledge support from the German Research Foundation (DFG) and Universität Leipzig within the program of Open Access Publishing.

ORCID iDs

Anna Hassa https://orcid.org/0000-0002-8087-6592
Marius Grundmann https://orcid.org/0000-0001-7554-182X
Holger von Wenckstern https://orcid.org/0000-0002-3936-275X

References

[1] Higashiwaki M, Murakami H, Kumagai Y and Kuramata A 2016 Current status of Ga_2O_3 power devices *Japan. J. Appl. Phys.* **55** 1202A1
[2] Stepanov S, Nikolaev V, Bougrov V and Romanov A 2016 Gallium oxide: properties and applications—a review *Rev. Adv. Mater. Sci.* **44** 63–86
[3] von Wenckstern H 2017 Group-III sesquioxides: growth, physical properties and devices *Adv. Electron. Mater.* **3** 1600350

[4] Pearton S J, Yang J, Cary P H, Ren F, Kim J, Tadjer M J and Mastro M A 2018 A review of Ga_2O_3 materials, processing and devices *Appl. Phys. Rev.* **5** 011301

[5] Zhang J, Shi J, Qi D-C, Chen L and Zhang K H L 2020 Recent progress on the electronic structure, defect and doping properties of Ga_2O_3 *APL Mater.* **8** 020906

[6] Higashiwaki M, Kuramata A, Murakami H and Kumagai Y 2017 State-of-the-art technologies of gallium oxide power devices *J. Phys. D: Appl. Phys.* **50** 333002

[7] Zhang Z, von Wenckstern H and Grundmann M 2014 Monolithic multichannel ultraviolet photodiodes based on (Mg,Zn)O thin films with continuous composition spreads *IEEE J. Sel. Top. Quantum Electron.* **20** 106–11

[8] Bierwagen O 2015 Indium oxide—a transparent, wide-band gap semiconductor for (opto)electronic applications *Semicond. Sci. Technol.* **30** 024001

[9] Thune E, Fakih A, Matringe C, Babonneau D and Guinebretière R 2017 Understanding of one dimensional ordering mechanisms at the (001) sapphire vicinal surface *J. Appl. Phys.* **121** 015301

[10] Roy R, Hill V G and Osborn E F 1952 Polymorphism of Ga_2O_3 and the system Ga_2O_3-H_2O *J. Am. Chem. Soc.* **74** 719–22

[11] Playford H Y, Hannon A C, Tucker M G, Dawson D M, Ashbrook S E, Kastiban R J, Sloan J and Walton R I 2014 Characterization of structural disorder in γ-Ga_2O_3 *J. Phys. Chem.* C **118** 16188–98

[12] Müller H K 1968 Electrical and optical properties of sputtered In_2O_3 films. I. Electrical properties and intrinsic absorption *Phys. Status Solidi* b **27** 723–31

[13] Weiher R L and Ley R P 1966 Optical properties of indium oxide *J. Appl. Phys.* **37** 299–302

[14] King P D C *et al* 2009 Band gap, electronic structure and surface electron accumulation of cubic and rhombohedral In_2O_3 *Phys. Rev.* B **79** 205211

[15] Momma K and Izumi F 2011 VESTA 3 for three-dimensional visualization of crystal, volumetric and morphology data *J. Appl. Crystallogr.* **44** 1272–6

[16] Dobrovinskaya E R, Lytvynov L A and Pishchik V 2009 *Sapphire: Material, Manufacturing, Applications* (Berlin: Springer)

[17] Marezio M and Remeika J P 1967 Bond lengths in the α-Ga_2O_3 structure and the high-pressure phase of $Ga_{2-x}Fe_xO_3$ *J. Chem. Phys.* **46** 1862–5

[18] Prewitt C T, Shannon R D, Rogers D B and Sleight A W 1969 C rare earth oxide-corundum transition and crystal chemistry of oxides having the corundum structure *Inorg. Chem.* **8** 1985–93

[19] Zhou R-S and Snyder R L 1991 Structures and transformation mechanisms of the β, γ and θ transition aluminas *Acta Crystallogr.* B **47** 617–30

[20] Åhman J, Svensson G and Albertsson J 1996 A reinvestigation of β-gallium oxide *Acta Crystallogr.* C **52** 1336–8

[21] Ollivier B, Retoux R, Lacorre P, Massiot D and Férey G 1997 Crystal structure of κ-alumina: an x-ray powder diffraction, TEM and NMR study *J. Mater. Chem.* **7** 1049–56

[22] Cora I, Mezzadri F, Boschi F, Bosi M, Čaplovičová M, Calestani G, Dódony I, Pécz B and Fornari R 2017 The real structure of ε-Ga_2O_3 and its relation to κ-phase *CrystEngComm* **19** 1509–16

[23] Edwards D D, Folkins P E and Mason T O 1997 Phase equilibria in the Ga_2O_3 In_2O_3 system *J. Am. Ceram. Soc.* **80** 253–7

[24] Shinohara D and Fujita S 2008 Heteroepitaxy of corundum-structured α-Ga_2O_3 thin films on α-Al_2O_3 substrates by ultrasonic mist chemical vapor deposition *Japan. J. Appl. Phys.* **47** 7311

[25] Kawaharamura T, Dang G T and Furuta M 2012 Successful growth of conductive highly crystalline Sn-doped α-Ga_2O_3 thin films by fine-channel mist chemical vapor deposition *Japan. J. Appl. Phys.* **51** 040207

[26] Cuscó R, Domènech-Amador N, Hatakeyama T, Yamaguchi T, Honda T and Artús L 2015 Lattice dynamics of a mist-chemical vapor deposition-grown corundum-like Ga_2O_3 single crystal *J. Appl. Phys.* **117** 185706

[27] Kaneko K, Kawanowa H, Ito H and Fujita S 2012 Evaluation of misfit relaxation in α-Ga_2O_3 epitaxial growth on α-Al_2O_3 substrate *Japan. J. Appl. Phys.* **51** 020201

[28] Akaiwa K, Kaneko K, Ichino K and Fujita S 2016 Conductivity control of Sn-doped α-Ga_2O_3 thin films grown on sapphire substrates *Japan. J. Appl. Phys.* **55** 1202BA

[29] Shimazoe K, Nishinaka H, Arata Y, Tahara D and Yoshimoto M 2020 Phase control of α- and κ-Ga_2O_3 epitaxial growth on $LiNbO_3$ and $LiTaO_3$ substrates using α-Fe_2O_3 buffer layers *AIP Adv.* **10** 055310

[30] Dong Lee S, Kaneko K and Fujita S 2016 Homoepitaxial growth of beta gallium oxide films by mist chemical vapor deposition *Japan. J. Appl. Phys.* **55** 1202B8

[31] Tahara D, Nishinaka H, Morimoto S and Yoshimoto M 2017 Stoichiometric control for heteroepitaxial growth of smooth ε-Ga_2O_3 thin films on c-plane AlN templates by mist chemical vapor deposition *Japan. J. Appl. Phys.* **56** 078004

[32] Battiston G, Gerbasi R, Porchia M, Bertoncello R and Caccavale F 1996 Chemical vapour deposition and characterization of gallium oxide thin films *Thin Solid Films* **279** 115–18

[33] Kong L, Ma J, Luan C and Zhu Z 2011 Structural and optical properties of Ga_2O_3: in films deposited on MgO (100) substrates by MOCVD *J. Solid State Chem.* **184** 1946–50

[34] Mi W, Ma J, Luan C, Lv Y, Xiao H and Li Z 2012 Characterization of β-Ga_2O_3 epitaxial films grown on MgO (111) substrates by metal-organic chemical vapor deposition *Mater. Lett.* **87** 109–12

[35] Gogova D, Wagner G, Baldini M, Schmidbauer M, Irmscher K, Schewski R, Galazka Z, Albrecht M and Fornari R 2014 Structural properties of Si-doped β-Ga_2O_3 layers grown by MOVPE *J. Cryst. Growth* **401** 665–9

[36] Rafique S, Han L, Tadjer M J, Freitas J A, Mahadik N A and Zhao H 2016 Homoepitaxial growth of β-Ga_2O_3 thin films by low pressure chemical vapor deposition *Appl. Phys. Lett.* **108** 182105

[37] Baldini M, Albrecht M, Fiedler A, Irmscher K, Klimm D, Schewski R and Wagner G 2016 Semiconducting Sn-doped β-Ga_2O_3 homoepitaxial layers grown by metal organic vapour-phase epitaxy *J. Mater. Sci.* **51** 3650–6

[38] Zhuo Y, Chen Z, Tu W, Ma X, Pei Y and Wang G 2017 β-Ga_2O_3 versus ε-Ga_2O_3: control of the crystal phase composition of gallium oxide thin film prepared by metal-organic chemical vapor deposition *Appl. Surf. Sci.* **420** 802–7

[39] Chen Y, Xia X, Liang H, Abbas Q, Liu Y and Du G 2018 Growth pressure controlled nucleation epitaxy of pure phase ε- and β-Ga_2O_3 films on Al_2O_3 via MOCVD *Cryst. Growth Des.* **18** 1147–54

[40] Alema F, Hertog B, Osinsky A, Mukhopadhyay P, Toporkov M and Schoenfeld W V 2017 Fast growth rate of epitaxial β-Ga_2O_3 by close coupled showerhead MOCVD *J. Cryst. Growth* **475** 77–82

[41] Xia X, Chen Y, Feng Q, Liang H, Tao P, Xu M and Du G 2016 Hexagonal phase-pure wide band gap ε-Ga_2O_3 films grown on 6H-SiC substrates by metal organic chemical vapor deposition *Appl. Phys. Lett.* **108** 202103

[42] Mezzadri F, Calestani G, Boschi F, Delmonte D, Bosi M and Fornari R 2016 Crystal structure and ferroelectric properties of ε-Ga_2O_3 films grown on (0001)-sapphire *Inorg. Chem.* **55** 12079–84

[43] Pavesi M, Fabbri F, Boschi F, Piacentini G, Baraldi A, Bosi M, Gombia E, Parisini A and Fornari R 2018 ε-Ga_2O_3 epilayers as a material for solar-blind UV photodetectors *Mater. Chem. Phys.* **205** 502–7

[44] Mulazzi M, Reichmann F, Becker A, Klesse W M, Alippi P, Fiorentini V, Parisini A, Bosi M and Fornari R 2019 The electronic structure of ε-Ga_2O_3 *APL Mater.* **7** 022522

[45] Park S H, Lee H S, Ahn H S and Yang M 2019 Crystal phase control of ε-Ga_2O_3 fabricated using by metal-organic chemical vapor deposition *J. Korean Phys. Soc.* **74** 502–7

[46] Oshima Y, Víllora E G and Shimamura K 2015 Halide vapor phase epitaxy of twin-free α-Ga_2O_3 on sapphire (0001) substrates *Appl. Phys. Express* **8** 055501

[47] Oshima Y, Kawara K, Shinohe T, Hitora T, Kasu M and Fujita S 2019 Epitaxial lateral overgrowth of α-Ga_2O_3 by halide vapor phase epitaxy *APL Mater.* **7** 022503

[48] Pechnikov A I, Stepanov S I, Chikiryaka A V, Scheglov M P, Odnobludov M A and Nikolaev V I 2019 Thick α-Ga_2O_3 layers on sapphire substrates grown by halide epitaxy *Semiconductors* **53** 780–3

[49] Leach J H, Udwary K, Rumsey J, Dodson G, Splawn H and Evans K R 2019 Halide vapor phase epitaxial growth of β-Ga_2O_3 and α-Ga_2O_3 films *APL Mater.* **7** 022504

[50] Orita M, Ohta H, Hirano M and Hosono H 2000 Deep-ultraviolet transparent conductive β-Ga_2O_3 thin films *Appl. Phys. Lett.* **77** 4166–8

[51] Murakami H *et al* 2014 Homoepitaxial growth of β-Ga_2O_3 layers by halide vapor phase epitaxy *Appl. Phys. Express* **8** 015503

[52] Nomura K, Goto K, Togashi R, Murakami H, Kumagai Y, Kuramata A, Yamakoshi S and Koukitu A 2014 Thermodynamic study of β-Ga_2O_3 growth by halide vapor phase epitaxy *J. Cryst. Growth* **405** 19–22

[53] Oshima Y, Víllora E G and Shimamura K 2015 Quasi-heteroepitaxial growth of β-Ga_2O_3 on off-angled sapphire (0 0 0 1) substrates by halide vapor phase epitaxy *J. Cryst. Growth* **410** 53–8

[54] Nikolaev V, Pechnikov A, Stepanov S, Nikitina I, Smirnov A, Chikiryaka A, Sharofidinov S, Bougrov V and Romanov A 2016 Epitaxial growth of β-Ga_2O_3 on (0001) sapphire substrates by halide vapour phase epitaxy *Mater. Sci. Semicond. Process.* **47** 16–19

[55] Oshima Y, Víllora E G, Matsushita Y, Yamamoto S and Shimamura K 2015 Epitaxial growth of phase-pure ε-Ga_2O_3 by halide vapor phase epitaxy *J. Appl. Phys.* **118** 085301

[56] Nikolaev V I, Stepanov S I, Pechnikov A I, Shapenkov S, Scheglov M P, Chikiryaka A and Vyvenko O F 2020 HVPE growth and characterization of ε-Ga_2O_3 films on various substrates *ECS J. Solid State Sci. Technol.* **9** 045014

[57] Schewski R *et al* 2014 Epitaxial stabilization of pseudomorphic α-Ga_2O_3 on sapphire (0001) *Appl. Phys. Express* **8** 011101

[58] Gottschalch V, Merker S, Blaurock S, Kneiß M, Teschner U, Grundmann M and Krautscheid H 2019 Heteroepitaxial growth of α-, β-, γ- and κ-Ga_2O_3 phases by metalorganic vapor phase epitaxy *J. Cryst. Growth* **510** 76–84

[59] Wagner G, Baldini M, Gogova D, Schmidbauer M, Schewski R, Albrecht M, Galazka Z, Klimm D and Fornari R 2013 Homoepitaxial growth of β-Ga_2O_3 layers by metal-organic vapor phase epitaxy *Phys. Status Solidi* a **211** 27–33

[60] Orita M, Hiramatsu H, Ohta H, Hirano M and Hosono H 2002 Preparation of highly conductive, deep ultraviolet transparent β-Ga_2O_3 thin film at low deposition temperatures *Thin Solid Films* **411** 134–9

[61] Matsuzaki K, Hiramatsu H, Nomura K, Yanagi H, Kamiya T, Hirano M and Hosono H 2006 Growth, structure and carrier transport properties of Ga_2O_3 epitaxial film examined for transparent field-effect transistor *Thin Solid Films* **496** 37–41

[62] Petitmangin A, Hébert C, Perrière J, Gallas B, Binet L, Barboux P and Vermaut P 2011 Metallic clusters in nonstoichiometric gallium oxide films *J. Appl. Phys.* **109** 013711

[63] Hebert C, Petitmangin A, Perrière J, Millon E, Petit A, Binet L and Barboux P 2012 Phase separation in oxygen deficient gallium oxide films grown by pulsed-laser deposition *Mater. Chem. Phys.* **133** 135–9

[64] Petitmangin A, Gallas B, Hebert C, Perrière J, Binet L, Barboux P and Portier X 2013 Characterization of oxygen deficient gallium oxide films grown by PLD *Appl. Surf. Sci.* **278** 153–7

[65] Müller S, von Wenckstern H, Splith D, Schmidt F and Grundmann M 2014 Control of the conductivity of Si-doped β-Ga_2O_3 thin films via growth temperature and pressure *Phys. Status Solidi* a **211** 34–9

[66] Zhang F B, Saito K, Tanaka T, Nishio M and Guo Q X 2014a Structural and optical properties of Ga_2O_3 films on sapphire substrates by pulsed laser deposition *J. Cryst. Growth* **387** 96–100

[67] Seiler W, Selmane M, Abdelouhadi K and Perrière J 2015 Epitaxial growth of gallium oxide films on c-cut sapphire substrate *Thin Solid Films* **589** 556–62

[68] Leedy K D *et al* 2018 Si content variation and influence of deposition atmosphere in homoepitaxial Si-doped β-Ga_2O_3 films by pulsed laser deposition *APL Mater.* **6** 101102

[69] Kneiß M, Hassa A, Splith D, Sturm C, von Wenckstern H, Schultz T, Koch N, Lorenz M and Grundmann M 2019 Tin-assisted heteroepitaxial PLD-growth of κ-Ga_2O_3 thin films with high crystalline quality *APL Mater.* **7** 02251

[70] Oshima T, Okuno T and Fujita S 2007 Ga_2O_3 thin film growth on c-plane sapphire substrates by molecular beam epitaxy for deep-ultraviolet photodetectors *Japan. J. Appl. Phys.* **46** 7217–20

[71] Oshima T, Arai N, Suzuki N, Ohira S and Fujita S 2008 Surface morphology of homoepitaxial β-Ga_2O_3 thin films grown by molecular beam epitaxy *Thin Solid Films* **516** 5768–71

[72] Okumura H, Kita M, Sasaki K, Kuramata A, Higashiwaki M and Speck J S 2014 Systematic investigation of the growth rate of β-Ga_2O_3(010) by plasma-assisted molecular beam epitaxy *Appl. Phys. Express* **7** 095501

[73] Vogt P and Bierwagen O 2015 The competing oxide and sub-oxide formation in metal-oxide molecular beam epitaxy *Appl. Phys. Lett.* **106** 081910

[74] Mauze A, Zhang Y, Itoh T, Wu F and Speck J S 2020 Metal oxide catalyzed epitaxy (MOCATAXY) of β-Ga_2O_3 films in various orientations grown by plasma-assisted molecular beam epitaxy *APL Mater.* **8** 021104

[75] Vogt P, Brandt O, Riechert H, Lähnemann J and Bierwagen O 2017 Metal-exchange catalysis in the growth of sesquioxides: towards heterostructures of transparent oxide semiconductors *Phys. Rev. Lett.* **119** 196001

[76] Kracht M *et al* 2017 Tin-assisted synthesis of ε-Ga_2O_3 by molecular beam epitaxy *Phys. Rev. Appl.* **8** 054002

[77] won Choi D, Chung K-B and Park J-S 2013 Low temperature Ga_2O_3 atomic layer deposition using gallium tri-isopropoxide and water *Thin Solid Films* **546** 31–4

[78] Altuntas H, Donmez I, Ozgit-Akgun C and Biyikli N 2014 Electrical characteristics of β-Ga_2O_3 thin films grown by PEALD *J. Alloys Compd.* **593** 190–5

[79] Boschi F, Bosi M, Berzina T, Buffagni E, Ferrari C and Fornari R 2016 Hetero-epitaxy of ε-Ga_2O_3 layers by MOCVD and ALD *J. Cryst. Growth* **443** 25–30

[80] Kaneko K, Fujita S and Hitora T 2018 A power device material of corundum-structured α-Ga_2O_3 fabricated by MIST EPITAXY® technique *Japan. J. Appl. Phys.* **57** 02CB18

[81] Sinha G, Adhikary K and Chaudhuri S 2005 Sol–gel derived phase pure α-Ga_2O_3 nanocrystalline thin film and its optical properties *J. Cryst. Growth* **276** 204–7

[82] Li S, Jiao S, Wang D, Gao S and Wang J 2018 The influence of sputtering power on the structural, morphological and optical properties of β-Ga_2O_3 thin films *J. Alloys Compd.* **753** 186–91

[83] Ueda N, Hosono H, Waseda R and Kawazoe H 1997 Synthesis and control of conductivity of ultraviolet transmitting β-Ga_2O_3 single crystals *Appl. Phys. Lett.* **70** 3561–3

[84] Víllora E G, Shimamura K, Yoshikawa Y, Aoki K and Ichinose N 2004 Large-size β-Ga_2O_3 single crystals and wafers *J. Cryst. Growth* **270** 420–6

[85] Suzuki N, Ohira S, Tanaka M, Sugawara T, Nakajima K and Shishido T 2007 Fabrication and characterization of transparent conductive Sn-doped β-Ga_2O_3 single crystal *Phys. Status Solidi* c **4** 2310–13

[86] Aida H, Nishiguchi K, Takeda H, Aota N, Sunakawa K and Yaguchi Y 2008 Growth of β-Ga_2O_3 single crystals by the edge-defined, film fed growth method *Japan. J. Appl. Phys.* **47** 8506–9

[87] Tomm Y, Reiche P, Klimm D and Fukuda T 2000 Czochralski grown Ga_2O_3 crystals *J. Cryst. Growth* **220** 510–14

[88] Galazka Z *et al* 2010 Czochralski growth and characterization of β-Ga_2O_3 single crystals *Cryst. Res. Technol.* **45** 1229–36

[89] Lorenz M, Woods J and Gambino R 1967 Some electrical properties of the semiconductor β-Ga_2O_3 *J. Phys. Chem. Solids* **28** 403–4

[90] Harwig T and Schoonman J 1978 Electrical properties of β-Ga_2O_3 single crystals. II *J. Solid State Chem.* **23** 205–11

[91] Schieber M 1964 Growth of oxide crystals by the flux method *J. Am. Ceram. Soc.* **47** 655

[92] Shannon R and Prewitt C 1968 Synthesis and structure of phases in the In_2O_3–Ga_2O_3 system *J. Inorg. Nucl. Chem.* **30** 1389–98

[93] Frank G, Brock L and Bausen H 1976 The solubilities of Sn in In_2O_3 and of In in SnO_2 crystals grown from Sn–In melts *J. Cryst. Growth* **36** 179–80

[94] Wang C Y *et al* 2006 Phase selective growth and properties of rhombohedral and cubic indium oxide *Appl. Phys. Lett.* **89** 011904

[95] Wang C Y, Lebedev V, Cimalla V, Kups T, Tonisch K and Ambacher O 2007 Structural studies of single crystalline In_2O_3 films epitaxially grown on InN (0001) *Appl. Phys. Lett.* **90** 221902

[96] Kong L, Ma J, Luan C, Zhu Z and Yu Q 2011 Domain structure and optical property of epitaxial indium oxide film deposited on MgO (100) substrate *Surf. Sci.* **605** 977–81

[97] Tarsa E J, English J H and Speck J S 1993 Pulsed laser deposition of oriented In_2O_3 on (001) InAs, MgO and yttria-stabilized zirconia *Appl. Phys. Lett.* **62** 2332–4

[98] Koida T and Kondo M 2006 High electron mobility of indium oxide grown on yttria-stabilized zirconia *J. Appl. Phys.* **99** 123703

[99] Park C-Y, Yoon S-G, Jo Y-H and Shin S-C 2009 Room-temperature ferromagnetism observed in Mo-doped indium oxide films *Appl. Phys. Lett.* **95** 122502

[100] Kranert C, Schmidt-Grund R and Grundmann M 2014 Raman active phonon modes of cubic In_2O_3 *Phys. Status Solidi (RRL)* **8** 554–9

[101] Schmidt-Grund R, Krauß H, Kranert C, Bonholzer M and Grundmann M 2014 Temperature dependence of the dielectric function in the spectral range (0.5–8.5) eV of an In_2O_3 thin film *Appl. Phys. Lett.* **105** 111906

[102] Taga N, Maekawa M, Shigesato Y, Yasui I, Kamei M and Haynes T E 1998 Deposition of heteroepitaxial In_2O_3 thin films by molecular beam epitaxy *Japan. J. Appl. Phys.* **37** 6524–9

[103] Bourlange A, Payne D J, Egdell R G, Foord J S, Edwards P P, Jones M O, Schertel A, Dobson P J and Hutchison J L 2008 Growth of In_2O_3 (100) on Y-stabilized ZrO_2 (100) by O-plasma assisted molecular beam epitaxy *Appl. Phys. Lett.* **92** 092117

[104] Morales E H, He Y, Vinnichenko M, Delley B and Diebold U 2008 Surface structure of Sn-doped In_2O_3 (111) thin films by STM *New J. Phys.* **10** 125030

[105] Bierwagen O, White M E, Tsai M-Y and Speck J S 2009 Plasma-assisted molecular beam epitaxy of high quality In_2O_3 (001) thin films on Y-stabilized ZrO_2 (001) using In as an auto surfactant *Appl. Phys. Lett.* **95** 262105

[106] Bierwagen O and Speck J S 2010 Nucleation of islands and continuous high-quality In_2O_3 (001) films during plasma-assisted molecular beam epitaxy on Y-stabilized ZrO_2 (001) *J. Appl. Phys.* **107** 113519

[107] Zhang K H L, Lazarov V K, Galindo P L, Oropeza F E, Payne D J, Lai H H-C and Egdell R G 2012 Domain matching epitaxial growth of In_2O_3 thin films on α-Al_2O_3 (0001) *Cryst. Growth Des.* **12** 1000–7

[108] Kamei M, Shigesato Y and Takaki S 1995 Origin of characteristic grain-subgrain structure of tin-doped indium oxide films *Thin Solid Films* **259** 38–45

[109] Taga N, Odaka H, Shigesato Y, Yasui I, Kamei M and Haynes T E 1996 Electrical properties of heteroepitaxial grown tin-doped indium oxide films *J. Appl. Phys.* **80** 978–84

[110] Xirouchaki C, Kiriakidis G, Pedersen T F and Fritzsche H 1996 Photoreduction and oxidation of as-deposited microcrystalline indium oxide *J. Appl. Phys.* **79** 9349–52

[111] Galazka Z *et al* 2013 Melt growth, characterization and properties of bulk In_2O_3 single crystals *J. Cryst. Growth* **362** 349–52

[112] Ito H, Kaneko K and Fujita S 2012 Growth and band gap control of corundum-structured α-$(AlGa)_2O_3$ thin films on sapphire by spray-assisted mist chemical vapor deposition *Japan. J. Appl. Phys.* **51** 100207

[113] Fujita S and Kaneko K 2014 Epitaxial growth of corundum-structured wide band gap III-oxide semiconductor thin films *J. Cryst. Growth* **401** 588–92

[114] Kaneko K, Suzuki K, Ito Y and Fujita S 2016 Growth characteristics of corundum-structured α-$(Al_xGa_{1-x})_2O_3$/Ga_2O_3 heterostructures on sapphire substrates *J. Cryst. Growth* **436** 150–4

[115] Dang G T, Yasuoka T, Tagashira Y, Tadokoro T, Theiss W and Kawaharamura T 2018 Bandgap engineering of α-$(Al_xGa_{1-x})_2O_3$ by a mist chemical vapor deposition two-chamber system and verification of Vegard's Law *Appl. Phys. Lett.* **113** 062102

[116] Lorenz M, Hohenberger S, Rose E and Grundmann M 2018 Atomically stepped, pseudomorphic, corundum-phase $(Al_{1-x}Ga_x)_2O_3$ thin films ($0 \leq x < 0.08$) grown on R-plane sapphire *Appl. Phys. Lett.* **113** 231902

[117] Grundmann M and Lorenz M 2020 Anisotropic strain relaxation through prismatic and basal slip in α-$(Al,Ga)_2O_3$ on R-plane Al_2O_3 *APL Mater.* **8** 021108

[118] Hassa A, Storm P, Kneiß M, Splith D, von Wenckstern H, Lorenz M and Grundmann M 2020 Structural and elastic

properties of α-$(Al_xGa_{1-x})_2O_3$ thin films on (11.0) Al_2O_3 substrates for the entire composition range *Phys. Status Solidi* b **258** 2000394
[119] Kumaran R, Tiedje T, Webster S E, Penson S and Li W 2010 Epitaxial Nd-doped α-$(Al_{1-x}Ga_x)_2O_3$ films on sapphire for solid-state waveguide lasers *Opt. Lett.* **35** 3793
[120] Suzuki N, Kaneko K and Fujita S 2014 Growth of corundum-structured $(In_xGa_{1-x})_2O_3$ alloy thin films on sapphire substrates with buffer layers *J. Cryst. Growth* **401** 670–2
[121] Fujita S, Oda M, Kaneko K and Hitora T 2016 Evolution of corundum-structured III-oxide semiconductors: growth, properties and devices *Japan. J. Appl. Phys.* 1 **55** 1202A3
[122] Zhang F, Saito K, Tanaka T, Nishio M, Arita M and Guo Q 2014 Wide bandgap engineering of $(AlGa)_2O_3$ films *Appl. Phys. Lett.* **105** 162107
[123] Wakabayashi R, Oshima T, Hattori M, Sasaki K, Masui T, Kuramata A, Yamakoshi S, Yoshimatsu K and Ohtomo A 2015 Oxygen-radical-assisted pulsed-laser deposition of β-Ga_2O_3 and β-$(Al_xGa_{1-x})_2O_3$ films *J. Cryst. Growth* **424** 77–9
[124] Wang X, Chen Z, Zhang F, Saito K, Tanaka T, Nishio M and Guo Q 2016 Influence of substrate temperature on the properties of $(AlGa)_2O_3$ thin films prepared by pulsed laser deposition *Ceram. Int.* **42** 12783–8
[125] Feng Q, Feng Z, Hu Z, Xing X, Yan G, Zhang J, Xu Y, Lian X and Hao Y 2018 Temperature dependent electrical properties of pulse laser deposited Au/Ni/β-$(AlGa)_2O_3$ Schottky diode *Appl. Phys. Lett.* **112** 072103
[126] Vaidya A *et al* 2019 Structural, band and electrical characterization of β-$(Al_{0.19}Ga_{0.81})_2O_3$ films grown by molecular beam epitaxy on Sn doped β-Ga_2O_3 substrate *J. Appl. Phys.* **126** 095702
[127] Okumura H, Kato Y, Oshima T and Palacios T 2019 Demonstration of lateral field-effect transistors using Sn-doped β-$(AlGa)_2O_3$ (010) *Japan. J. Appl. Phys.* **58** SBBD12
[128] Oshima T, Okuno T, Arai N, Kobayashi Y and Fujita S 2009 β-$Al_{2x}Ga_{2-2x}O_3$ thin film growth by molecular beam epitaxy *Japan. J. Appl. Phys.* **48** 070202
[129] Ahmadi E, Oshima Y, Wu F and Speck J S 2017 Schottky barrier height of Ni to β-$(Al_xGa_{1-x})_2O_3$ with different compositions grown by plasma-assisted molecular beam epitaxy *Semicond. Sci. Technol.* **32** 035004
[130] Wang C-C, Yuan S-H, Ou S-L, Huang S-Y, Lin K-Y, Chen Y-A, Hsiao P-W and Wuu D-S 2018 Growth and characterization of co-sputtered aluminum-gallium oxide thin films on sapphire substrates *J. Alloys Compd.* **765** 894–900
[131] Baldini M, Gogova D, Irmscher K, Schmidbauer M, Wagner G and Fornari R 2014 Heteroepitaxy of $Ga_{2(1-x)}In_{2x}O_3$ layers by MOVPE with two different oxygen sources *Cryst. Res. Technol.* **49** 552–7
[132] von Wenckstern H, Splith D, Werner A, Müller S, Lorenz M and Grundmann M 2015 Properties of schottky barrier diodes on $(In_xGa_{1-x})_2O_3$ for $0.01 \leq x \leq 0.85$ determined by a combinatorial approach *ACS Comb. Sci.* **17** 710–15
[133] von Wenckstern H, Splith D, Purfürst M, Zhang Z, Kranert C, Müller S, Lorenz M and Grundmann M 2015 Structural and optical properties of $(In,Ga)_2O_3$ thin films and characteristics of Schottky contacts thereon *Semicond. Sci. Technol.* **30** 024005
[134] Zhang F, Saito K, Tanaka T, Nishio M and Guo Q 2014 Wide bandgap engineering of $(GaIn)_2O_3$ films *Solid State Commun.* **186** 28–31
[135] Zhang Z, von Wenckstern H, Lenzner J, Lorenz M and Grundmann M 2016 Visible-blind and solar-blind ultraviolet photodiodes based on $(In_xGa_{1-x})_2O_3$ *Appl. Phys. Lett.* **108** 123503
[136] Vogt P and Bierwagen O 2016 Kinetics versus thermodynamics of the metal incorporation in molecular beam epitaxy of $(In_xGa_{1-x})_2O_3$ *APL Mater.* **4** 086112
[137] Kokubun Y, Abe T and Nakagomi S 2010 Sol–gel prepared $(Ga_{1-x}In_x)_2O_3$ thin films for solar-blind ultraviolet photodetectors *Phys. Status Solidi* a **207** 1741–5
[138] Oshima T and Fujita S 2008 Properties of Ga_2O_3-based $(In_xGa_{1-x})_2O_3$ alloy thin films grown by molecular beam epitaxy *Phys. Status Solidi* c **5** 3113–15
[139] Tahara D, Nishinaka H, Morimoto S and Yoshimoto M 2018 Heteroepitaxial growth of ε-$(Al_xGa_{1-x})_2O_3$ alloy films on c-plane AlN templates by mist chemical vapor deposition *Appl. Phys. Lett.* **112** 152102
[140] Storm P, Kneiß M, Hassa A, Schultz T, Splith D, von Wenckstern H, Koch N, Lorenz M and Grundmann M 2019 Epitaxial κ-$(Al_xGa_{1-x})_2O_3$ thin films and heterostructures grown by tin-assisted VCCS-PLD *APL Mater.* **7** 111110
[141] Hassa A, Sturm C, Kneiß M, Splith D, von Wenckstern H, Schultz T, Koch N, Lorenz M and Grundmann M 2020 Solubility limit and material properties of a κ-$(Al_xGa_{1-x})_2O_3$ thin film with a lateral cation gradient on (00.1)Al_2O_3 by tin-assisted PLD *APL Mater.* **8** 021103
[142] Hassa A, Wouters C, Kneiß M, Splith D, Sturm C, von Wenckstern H, Albrecht M, Lorenz M and Grundmann M 2020 Control of phase formation of $(Al_xGa_{1-x})_2O_3$ thin films on c-plane Al_2O_3 *J. Phys. D: Appl. Phys.* **53** 485105
[143] Nishinaka H, Miyauchi N, Tahara D, Morimoto S and Yoshimoto M 2018 Incorporation of indium into ε-gallium oxide epitaxial thin films grown via mist chemical vapour deposition for bandgap engineering *CrystEngComm* **20** 1882–8
[144] Hassa A, von Wenckstern H, Splith D, Sturm C, Kneiß M, Prozheeva V and Grundmann M 2019 Structural, optical and electrical properties of orthorhombic κ-$(In_xGa_{1-x})_2O_3$ thin films *APL Mater.* **7** 022525
[145] Kneiß M, Hassa A, Splith D, Sturm C, von Wenckstern H, Lorenz M and Grundmann M 2019 Epitaxial stabilization of single phase κ-$(In_xGa_{1-x})_2O_3$ thin films up to $x = 0.28$ on c-sapphire and κ-Ga_2O_3 (001) templates by tin-assisted VCCS-PLD *APL Mater.* **7** 101102
[146] Yang F, Ma J, Luan C and Kong L 2009 Structural and optical properties of $Ga_{2(1-x)}In_{2x}O_3$ films prepared on α-Al_2O_3 (0001) by MOCVD *Appl. Surf. Sci.* **255** 4401–4
[147] Kong L, Ma J, Yang F, Luan C and Zhu Z 2010 Preparation and characterization of $Ga_{2x}In_{2(1-x)}O_3$ films deposited on ZrO_2 (100) substrates by MOCVD *J. Alloys Compd.* **499** 75–9
[148] von Wenckstern H, Zhang Z, Schmidt F, Lenzner J, Hochmuth H and Grundmann M 2013 Continuous composition spread using pulsed-laser deposition with a single segmented target *CrystEngComm* **15** 10020
[149] von Wenckstern H, Kneiß M, Hassa A, Storm P, Splith D and Grundmann M 2019 A review of the segmented-target approach to combinatorial material synthesis by pulsed-laser deposition *Phys. Status Solidi* b **257** 1900626
[150] Lorenz M 2007 Pulsed laser deposition of ZnO-based thin films *Transparent Conductive Zinc Oxide: Basics and Applications in Thin Film Solar Cells, Springer Series in Materials Science Book 104* (Berlin: Springer) pp 303–57
[151] Hassa A, von Wenckstern H, Vines L and Grundmann M 2019 Influence of oxygen pressure on growth of Si-doped β-$(Al_xGa_{1-x})_2O_3$ thin films on c-sapphire substrates by pulsed laser deposition *ECS J. Solid State Sci. Technol.* **8** Q3217–20
[152] Kranert C, Lenzner J, Jenderka M, Lorenz M, von Wenckstern H, Schmidt-Grund R and Grundmann M

2014 Lattice parameters and Raman-active phonon modes of $(In_xGa_{1-x})_2O_3$ for $x < 0.4$ *J. Appl. Phys.* **116** 013505
[153] Kranert C, Jenderka M, Lenzner J, Lorenz M, von Wenckstern H, Schmidt-Grund R and Grundmann M 2015 Lattice parameters and Raman-active phonon modes of β-$(Al_xGa_{1-x})_2O_3$ *J. Appl. Phys.* **117** 125703
[154] Krueger B W, Dandeneau C S, Nelson E M, Dunham S T, Ohuchi F S, Olmstead M A and Jones J 2016 Variation of band gap and lattice parameters of β-$(Al_xGa_{1-x})_2O_3$ powder produced by solution combustion synthesis *J. Am. Ceram. Soc.* **99** 2467–73
[155] Vasyltsiv V I, Rym Y I and Zakharko Y M 1996 Optical absorption and photoconductivity at the band edge of β-$Ga_{2-x}In_xO_3$ *Phys. Status Solidi* b **195** 653–8
[156] Geller S 1960 Crystal structure of β-Ga_2O_3 *J. Chem. Phys.* **33** 676–84
[157] Jaromin A L and Edwards D D 2005 Subsolidus phase relationships in the Ga_2O_3-Al_2O_3-TiO_2 system *J. Am. Ceram. Soc.* **88** 2573–7
[158] Marezio M 1966 Refinement of the crystal structure of In_2O_3 at two wavelengths *Acta Crystallogr.* **20** 723–8
[159] Regoutz A, Egdell R, Morgan D, Palgrave R, Téllez H, Skinner S, Payne D, Watson G and Scanlon D 2015 Electronic and surface properties of Ga-doped In_2O_3 ceramics *Appl. Surf. Sci.* **349** 970–82
[160] Schmidt-Grund R, Kranert C, von Wenckstern H, Zviagin V, Lorenz M and Grundmann M 2015 Dielectric function in the spectral range (0.5–8.5)eV of an $(Al_xGa_{1-x})_2O_3$ thin film with continuous composition spread *J. Appl. Phys.* **117** 165307
[161] Feng Z, Feng Q, Zhang J, Li X, Li F, Huang L, Chen H-Y, Lu H-L and Hao Y 2018 Band alignment of $SiO_2/(Al_xGa_{1-x})_2O_3$ $(0 \leqslant x \leqslant 0.49)$ determined by X-ray photoelectron spectroscopy *Appl. Surf. Sci.* **434** 440–4
[162] Yourdshahyan Y, Ruberto C, Bengtsson L and Lundqvist B I 1997 First-principles calculations on the atomic and electronic structure of κ-Al_2O_3 *Phys. Rev.* B **56** 8553–8
[163] Walsh A *et al* 2008 Nature of the band gap of In_2O_3 revealed by first-principles calculations and x-ray spectroscopy *Phys. Rev. Lett.* **100** 167402
[164] Köstlin H, Jost R and Lems W 1975 Optical and electrical properties of doped In_2O_3 films *Phys. Status Solidi* a **29** 87–93
[165] von Wenckstern H, Splith D and Grundmann M 2020 Pulsed laser deposition 2 *Gallium Oxide: Materials Properties, Crystal Growth, and Devices* ed M Higashiwaki and S Fujita (Berlin: Springer) pp 273–91
[166] Sturm C, Schmidt-Grund R, Kranert C, Furthmüller J, Bechstedt F and Grundmann M 2016 Dipole analysis of the dielectric function of color dispersive materials: application to monoclinic Ga_2O_3 *Phys. Rev.* B **94** 035148
[167] Mo S-D and Ching W Y 1998 Electronic and optical properties of θ-Al_2O_3 and comparison to α-Al_2O_3 *Phys. Rev.* B **57** 15219–28
[168] Peelaers H, Steiauf D, Varley J B, Janotti A and de Walle C G V 2015 $(In_xGa_{1-x})_2O_3$ alloys for transparent electronics *Phys. Rev.* B **92** 085206